

A finite element model for high enthalpy two-phase flow in geothermal wellbores

Akbar, S.; Fathianpour, N.; Al Khoury, R.

DOI

[10.1016/j.renene.2016.03.034](https://doi.org/10.1016/j.renene.2016.03.034)

Publication date

2016

Document Version

Accepted author manuscript

Published in

Renewable Energy

Citation (APA)

Akbar, S., Fathianpour, N., & Al Khoury, R. (2016). A finite element model for high enthalpy two-phase flow in geothermal wellbores. *Renewable Energy*, 94, 223-236. <https://doi.org/10.1016/j.renene.2016.03.034>

Important note

To cite this publication, please use the final published version (if applicable).
Please check the document version above.

Copyright

Other than for strictly personal use, it is not permitted to download, forward or distribute the text or part of it, without the consent of the author(s) and/or copyright holder(s), unless the work is under an open content license such as Creative Commons.

Takedown policy

Please contact us and provide details if you believe this document breaches copyrights.
We will remove access to the work immediately and investigate your claim.

A finite element model for high enthalpy two-phase flow in geothermal wellbores

S. Akbar^{1,2,*}, N. Fathianpour¹, R. Al Khoury²

¹ Faculty of mining Engineering, Isfahan University of technology, PO Box 8415683111, Isfahan, Iran.

² Faculty of Civil Engineering and Geosciences, Delft University of Technology, PO Box 5048, 2600 GA Delft, the Netherlands

* Corresponding author: Tel.: +31 644338941. E-mail address: sa.3761@gmail.com (S. Akbar).

Abstract

This paper introduces a computational model for transient high enthalpy fluid flow through geothermal wellbores. The drift-flux model is utilized to formulate the physical behavior of fluid, and the constitutive relationships are described using relevant equations of state and empirical relationships. The governing equations are solved using the finite element method. All important physical phenomena and processes occurring along the wellbore, including buoyancy, phase change, compressibility, thermal interaction, wall friction and slip between phases are considered. Airlifting of water and air, initially existing in the wellbore before production, is also considered. During airlifting and early stages of production, two fluids exist along the wellbore: airlifted water-dry air fluid, and reservoir water-vapor fluid; giving rise to a discontinuity in thermodynamic properties between the two fluids. The discontinuity is modeled using the level-set method. Two numerical examples illustrating the computational capability and accuracy of the model are presented. The physical phenomena occurring during airlifting and production along the wellbore are highlighted.

Keywords: High enthalpy geothermal systems, wellbore, drift-flux model, level set, airlift.

1 Introduction

With the growing demand of renewable energy and the associated growth of interest and investment in geothermal energy extraction, the development of computational models for the simulation of a wide range of geothermal systems is inevitable. Predicting the fluid properties along the wellbore, such as temperature, phase composition and mass density is vital for the design and monitoring of geothermal systems. This constitutes the main objective of this research work, which aims at the development of a computational tool for deep high enthalpy geothermal systems consisting of multilevel geothermal reservoirs operated by multiple wellbores.

In deep high enthalpy geothermal systems, the fluid along the wellbore exhibits phase change, manifested by flash evaporation due to pressure reduction accompanied by a certain range of temperature. Below the flash evaporation point, in the upstream, the fluid is liquid, while immediately above it, the fluid is a mixture of water liquid and vapor. This sudden change in

38 material composition can cause significant change in its properties and behavior. Such kind of
39 physical behavior is computationally challenging and demanding. It requires innovative
40 conceptual modeling, descriptive mathematical formulation and robust numerical
41 discretization.

42 Several geothermal models and simulators are available in literature. Pioneering works have
43 been introduced by Poettmann and Carpenter (1952), Zuber and Findlay (1965) and Gould
44 (1974), who simulated steady-state heat and fluid flow in wellbores with two separated phases
45 with slip between them [1-3]. Miller (1980) was one of the first to developed a transient
46 wellbore simulator, WELBORE [4, 5]. Bjornsson and Bodvarsson (1987) stimulated one and two
47 phase flow along a vertical wellbore with multiple feed zones, and developed HOLA code,
48 which later on expanded to handle CO₂-H₂O and NaCl-H₂O systems [6, 7]. Gudmundsdottir et
49 al. (2013) developed a steady state model for one and two sliding separated phase flow along a
50 wellbore, and compared their results with measured data and existing models [8]. These
51 models, and most of existing simulators, are based on the finite difference or finite volume
52 methods. On the other hand, Saeid et al. (2013) introduced a finite element model for low
53 enthalpy deep geothermal systems [9].

54 Here, we solve the heat and fluid flow in a high enthalpy deep geothermal wellbore using the
55 finite element method. We utilize the drift-flux model [10-13] to simulate transient heat flow of
56 a compressible, two-phase fluid travelling along the wellbore. This model adopts the area-
57 averaged approach, where detailed analysis of the local behavior of the involved phases are
58 averaged over the cross-sectional area of the wellbore [14]. All important physical phenomena
59 and processes occurring along the wellbore, including fluid dynamics, buoyancy, phase change,
60 compressibility, thermal interaction, wall friction and slip between phases are considered.
61 Airlifting of water and air, initially existing in the wellbore before production, is also considered.
62 Airlifting is a process to facilitate fluid production by injecting air into an existing fluid to reduce
63 its mass density. During early stages of production, two fluids exist along the wellbore: the
64 wellbore airlifted water-dry air fluid, and the reservoir water-vapor fluid. This process
65 inevitably generates an interface between the two fluids that exhibits a jump in mass density,
66 specific enthalpy and other thermodynamic properties. The jump is modeled here using the
67 level-set method [15, 16], and coupled to the drift-flux model.

68 Numerical discretization of the mathematical model and implementation are conducted using
69 the finite element package COMSOL Multiphysics. As the model is compressible, highly
70 advective, non-linear and involves forces with opposite effects, such as buoyance that tempts
71 to force the fluid to flow against gravity, and drag forces that temp to impede the buoyance, it
72 is not possible to use the standard strong form implementation of the partial differential
73 equations in COMSOL. Instead, the weak form is implemented.

74 In this paper, we introduce a detailed formulation of the governing balance equations and their
75 relevant constitutive equations and equations of state. A detailed weak form formulation of the
76 governing partial differential equations, tailored for implementation in COMSOL, is also

77 introduced. We discuss the capability of the model to simulate heat and fluid flow in a vertical
 78 wellbore, which might be embedded in a wide range of high enthalpy reservoirs. Comparison to
 79 field data is also introduced.

80 **2 Mathematical model formulation**

81 The drift-flux model is utilized to formulate heat and fluid flow of a compressible two-phase
 82 mixture along a one-dimensional wellbore subjected to pumping at its upper boundary.
 83 Important aspects of fluid dynamics such as the inertia force, buoyancy, wall friction, drift
 84 velocity, flow profile, together with the jump in thermodynamic properties between the
 85 airlifted mixture and the reservoir mixture, are considered.

86 **2.1 Balance equations**

87 Using the drift-flux model, the transient fluid flow in a one-dimensional wellbore with a
 88 constant cross-sectional area can be described as

89 Mass balance

$$\frac{\partial \rho_m}{\partial t} + \frac{\partial \rho_m u_m}{\partial z} = 0 \quad (1)$$

90 Momentum balance

$$\frac{\partial \rho_m u_m}{\partial t} + \frac{\partial}{\partial z} (\rho_m u_m^2 + \gamma) = -\frac{\partial P}{\partial z} - \frac{f \rho_m |u_m| u_m}{4r_i} - \rho_m g \sin\theta \quad (2)$$

91 Energy balance

$$\frac{\partial}{\partial t} \left[\left(\rho_m h_m + \frac{\rho_m u_m^2}{2} \right) - P \right] + \frac{\partial}{\partial z} \left[\rho_m u_m \left(h_m + \frac{u_m^2}{2} \right) \right] = \frac{Q(z)}{\pi r_i^2} - \rho_m u_m g \sin\theta \quad (3)$$

92 where r_i is the inner radius of the wellbore, ρ_m is the fluid mixture density, u_m is the mixture
 93 velocity, P is the pressure, g is the gravitational constant, θ is the inclination angle of the
 94 wellbore, h_m is the specific enthalpy of the mixture, f is the wall friction coefficient, Q is the
 95 heat exchange between the wellbore and its surrounding formation, and γ is the slip between
 96 phases. Detailed formulation of f , Q and γ are given in Appendix A.

97 In hydrothermal high enthalpy systems, the thermodynamic state quantities, given in Eqs. (1)-
 98 3), play a major role in the fluid flow along the wellbore. The coupling between the fluid mass
 99 density, pressure, enthalpy, temperature and velocity significantly affect the mass and volume
 100 flow rates along the wellbore and, hence, the amount of energy production, which constitutes
 101 the main objectives of constructing geothermal energy systems. As the mass density and
 102 temperature are functions of pressure and specific enthalpy, and as the fluid velocity is
 103 important in determining the mass flow rate, we select the mixture pressure, P , specific
 104 enthalpy, h_m , and velocity, u_m , as the primary state variables. They are explicitly determined
 105 from solving the balance equations, Eqs. (1)-(3). The mass density and temperature are
 106 determined from the primary state variables via their equations of state and other relevant
 107 empirical relationships.

108 2.2 Constitutive equations

109 Physical characteristics of the formation water play a significant role on the flow along the
110 wellbore, and their good characterization is essential for the accuracy of computational results.
111 The mass density, in particular, plays a major role in determining the pressure and temperature
112 distribution along the wellbore, and together with the wall friction, slip between phases, and
113 thermal interaction with surrounding rock formation determine the mass and volume flow
114 rates.

115 The formation water mass density is a function of pressure, temperature, vapor volume
116 fraction and the type and amount of dissolved saline minerals and gases. The proposed model
117 is generic and can be tailored to a wide range of pressure and enthalpy, but for the current
118 research work, the focus is placed on the specific enthalpy range between 900 ($kJ\ kg^{-1}$) and
119 1100 ($kJ\ kg^{-1}$), and pressure range between 1 *bar* and 117 *bar*. In these ranges, for low saline
120 reservoirs, the salinity effect is not significant [17, 18], and accordingly, the properties of the
121 formation water can be described in terms of the equations of state of pure water. The
122 formation water is assumed a mixture of two phases: liquid water and vapor, which, depending
123 on the temperature and pressure, a single phase or both phases can exist in space.

124 Mixture mass density

125 The two-phase water mixture density is described as

$$\rho_m = \alpha \rho_g + (1 - \alpha) \rho_l \quad (4)$$

126 in which α is the vapor volume fraction, and ρ_g and ρ_l are the gas and liquid phase densities,
127 respectively, defined as

$$\rho_l(P, T) = 1 / \left(\frac{\partial g_1}{\partial P} \right)_T \quad (5)$$

$$\rho_g(P, T) = 1 / \left(\frac{\partial g_2}{\partial P} \right)_T \quad (6)$$

128 where g_1 and g_2 are the specific Gibbs free energy of the liquid and gas phases, respectively,
129 given in Appendix B.

130 The void fraction determines the volume occupied by vapor, making it an important parameter
131 in predicting the pressure drop along the wellbore. Rouhani and Axelsson (1970) proposed a
132 semi-empirical void fraction formulation, which is a function of vapor mass fraction, phases
133 densities and mass velocity, given as [19, 20]:

$$\alpha = \frac{X \rho_l}{C_0 X \rho_l + C_0 (1 - X) \rho_g + \frac{\rho_g \rho_l u_{gu}}{\rho_m u_m}} \quad (7)$$

134 where C_0 is the profile parameter, and u_{gu} is the drift flux velocity, given in details in Appendix
135 A. X is the vapor mass fraction, also known as the vapor quality, defined as

$$X = \frac{h_m - h_l}{h_g - h_l} \quad (8)$$

136 where h_l and h_g are the enthalpies of the liquid and gas phases, respectively, defined as:

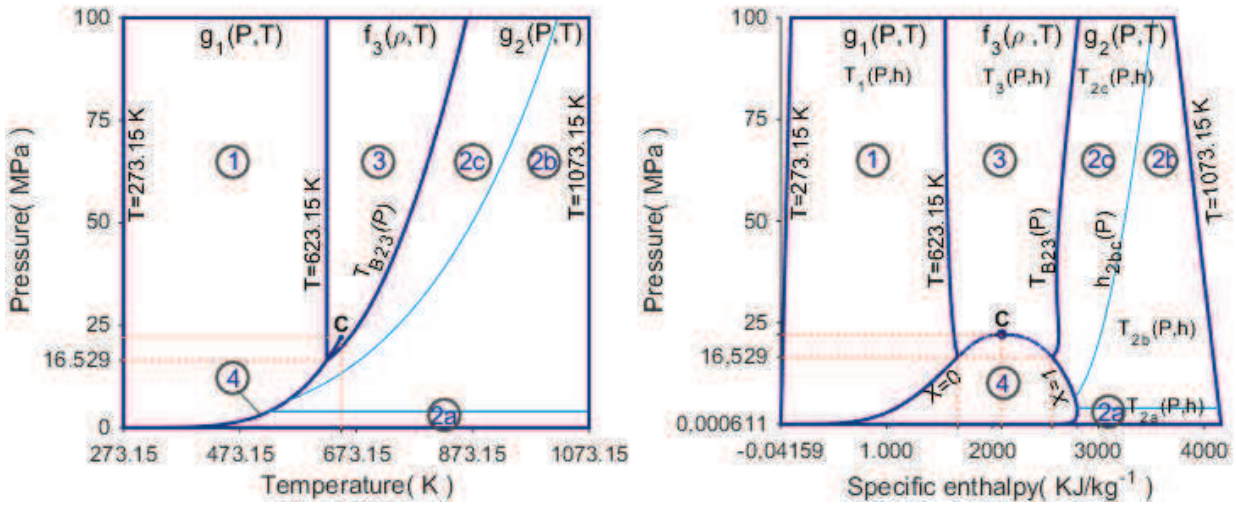
$$h_l(P, T) = g_1 - T \left(\frac{\partial g_1}{\partial T} \right)_P \quad (9)$$

$$h_g(P, T) = g_2 - T \left(\frac{\partial g_2}{\partial T} \right)_P \quad (10)$$

137 in which T is the temperature.

138 Mixture temperature

139 The mixture temperature distribution along the wellbore is considerably affected by the
 140 reservoir pressure and enthalpy. Reservoirs at different regions exhibit different ranges of
 141 pressure and enthalpy. Figure 1 shows the pressure-temperature and the pressure-specific
 142 enthalpy properties of pure water. They are described by four main regions, with region 2
 143 divided into three sub-regions. The regions are defined by the equations of state provided by
 144 the International Association for the Properties of Water and Steam (IAPWS). Here, the interest
 145 is on enthalpy and pressure ranges that generate liquid water, vapor and a mixture of them,
 146 namely, Regions 1, 2 and 4 in Figure 1.



147

148 **Figure 1: Pressure-temperature and pressure-specific enthalpy relationships of pure water, adopted**
 149 **from IAPWS-IF97 [21]**

150 According to Figure 1, the temperature is calculated using the following algorithm:

if $P \leq 16.529 \text{E}6$

 if $h_m \leq h_l(P, T_s(P))$ then $T = T_1$

 elseif $h_m \leq h_g(P, T_s(P))$ then $T = T_s$

 elseif $P \leq 4$ then $T = T_{2a}$

 elseif $h_m \leq h_{2bc}(P)$ then $T = T_{2c}$

 else $T = T_{2b}$

(11)

```

        end
    end
end
end
elseif  $h_m \leq h_l(P, 623.15)$  then  $T = T_1$ 
    else if  $h_m \geq h_g(P, T_{B23}(P))$ 
        if  $h_m \leq h_{2bc}(P)$  then  $T = T_{2c}$ 
            else  $T = T_{2b}$ 
        end
    else if  $P \leq P_{s3}(h)$  then  $T = T_s$ 
        else  $T = T_3$ 
    end
end
end
end

```

151 where the temperature is in Kelvin, P in Pa and h_m in $J kg^{-1}$. In Eq. (11), h_l and h_g are
 152 described in Eqs. (9) and (10), respectively; T_1 is the liquid temperature, given by

$$T_1(P, h_m) = \sum_{i=1}^{20} n_i \left(\frac{P}{1E6} \right)^{I_i} \left(\frac{h_m}{2.5E6} + 1 \right)^{J_i} \quad (12)$$

153 T_{2a} , T_{2b} and T_{2c} are the gas phase temperature in sub-regions 2a, 2b and 2c (Figure 1), given,
 154 respectively, by

$$T_{2a}(P, h_m) = \sum_{i=1}^{34} n_i \left(\frac{P}{1E6} \right)^{I_i} \left(\frac{h_m}{2E6} - 2.1 \right)^{I_i} \quad (13)$$

$$T_{2b}(P, h_m) = \sum_{i=1}^{38} n_i \left(\frac{P}{1E6} - 2 \right)^{I_i} \left(\frac{h_m}{2E6} - 2.6 \right)^{I_i} \quad (14)$$

$$T_{2c}(P, h_m) = \sum_{i=1}^{23} n_i \left(\frac{P}{1E6} + 25 \right)^{I_i} \left(\frac{h_m}{2E6} - 1.8 \right)^{I_i} \quad (15)$$

155 T_s is the saturation temperature, a function of saturation pressure P_s , belongs to the two-
 156 phase zone, region 4 (Figure 1), given by the quadratic equation [21]:
 157

$$\begin{aligned}
 & P_s^{0.5} \left(T_s + \frac{n_9}{T_s - n_{10}} \right)^2 + n_1 P_s^{0.5} \left(T_s + \frac{n_9}{T_s - n_{10}} \right) + n_2 P_s^{0.5} \\
 & \quad + n_3 P_s^{0.25} \left(T_s + \frac{n_9}{T_s - n_{10}} \right)^2 + n_4 P_s^{0.25} \left(T_s + \frac{n_9}{T_s - n_{10}} \right) \\
 & \quad + n_5 P_s^{0.25} + n_6 \left(T_s + \frac{n_9}{T_s - n_{10}} \right)^2 + n_7 \left(T_s + \frac{n_9}{T_s - n_{10}} \right) + n_8 \\
 & = 0
 \end{aligned} \quad (16)$$

158 T_3 is the water temperature in region 3 (Figure 1). The temperature in this region is more than
 159 350 °C, which is beyond the scope of the applications in this work.

160 T_{B23} is the water temperature at the boundary line between region 2 and region 3 in Figure 1,
 161 defined as

$$T_{B23}(P) = n_4 + \left[\left(\frac{P}{1E6} - n_5 \right) / n_3 \right]^{0.5} \quad (17)$$

162
 163 h_{2bc} is the specific enthalpy of the cross-border of region 2, given by

$$h_{2bc}(P) = 1000 \left(n'_4 + \left[\left(\frac{P}{1E6} - n'_5 \right) / n'_3 \right]^{0.5} \right) \quad (18)$$

164 and P_{s3} is the pressure at the boundary line between region 3 and region 4, given by

$$P_{s,3}(h_m) = \sum_{i=1}^{14} 22 * 10^6 * n_i \left(\frac{h_m}{2.6E6} - 1.02 \right)^{I_i} \left(\frac{h_m}{2.6E6} - 0.608 \right)^{J_i} \quad (19)$$

165 where the coefficient $n_i, n_i^0, n'_i, I_i, J_i, J_i^0$ can be found in IAPWS-IF97 [21].

166 **Other constitutive relationships**

167 Constitutive relationships for the mixture specific isobaric heat capacity (C_{p_m}), dynamic
 168 viscosity (μ_m) and thermal conductivity (λ_m) are given in Appendix A.

169 **2.3 Initial and boundary conditions**

170 Initially, the primary state variables might be described as

$$G(z, 0) = G_0(z) \quad \text{at } t = 0 \quad (20)$$

171 where G could be P, u_m or h_m .

172 The Dirichlet boundary conditions can be described as

$$G(z, t) = \hat{G}(z, t) \quad \text{on } \Gamma \quad (21)$$

173 in which Γ is a boundary in the physical system.

174 The Neumann boundary conditions are defined as

$$\begin{aligned} \hat{q}_\rho &= (\hat{\rho}_m \hat{u}_m) \cdot \mathbf{n} \\ \hat{q}_u &= (\hat{\rho}_m \hat{u}_m^2 + \hat{p}) \cdot \mathbf{n} \quad \text{on } \Gamma_q \\ \hat{q}_e &= \left(\hat{\rho}_m \hat{u}_m \left(\hat{h}_m + \frac{\hat{u}_m^2}{2} \right) \right) \cdot \mathbf{n} \end{aligned} \quad (22)$$

175 where Γ_q is the Neumann boundary, and the subscripts $\rho, u,$ and e refer to the mass,
 176 momentum, and energy balance equations, respectively.

177 **3 Numerical model formulation**

178 The governing equations are solved using the finite element method. The finite element
 7

179 package, COMSOL Multiphysics, is utilized as a framework for implementing and discretizing
180 the governing equations.

181 The governing drift-flux equations, Eqs. (1)-(11), together with the initial and boundary
182 conditions, Eqs.(21)-(22), form an initial and boundary value problem that is dynamic,
183 advective, nonlinear and involves phase change, together with buoyancy, friction and slip
184 forces. Solving such a problem using standard strong form implementation in COMSOL, as given
185 by the “Physics” option, entails utilization of excessively fine meshes and small time steps, but
186 yet, the calculation can be unstable and non-convergent. To tackle this, we solve the problem
187 by formulating the weak forms of the governing equations using the weighted residual finite
188 element method, and inserting them into COMSOL via the “PDE Interface”.

189 3.1 Weak form formulation

190 Using the weighted residual finite element method, the balance equations (1), (2) and (3),
191 together with the boundary conditions , Eqs.(21)-(22), can be described as

192 Mass balance

$$\int_L W \left(\frac{\partial \rho_m}{\partial t} + \frac{\partial \rho_m u_m}{\partial z} \right) dz = 0$$

193 where W is the weighting function and L is the element length. Solving the involved product
194 derivatives, applying the Green’s function, and imposing the Neumann-boundary condition (the
195 first equation in Eq. (22)), the weak form of the mass balance equation can be described as

$$\int_L W \frac{\partial \rho_m}{\partial t} dz - \int_L \rho_m u_m \frac{\partial W}{\partial z} dz + W \hat{q}_\rho |_{r_q} = 0 \quad (23)$$

196 Momentum balance

$$\int_L W \left(\rho_m \frac{\partial u_m}{\partial t} + u_m \frac{\partial \rho_m}{\partial t} + \frac{\partial \rho_m u_m^2}{\partial z} + \frac{\partial \gamma}{\partial z} + \frac{\partial P}{\partial z} + \rho g \sin\theta + \frac{f \rho_m |u_m| u_m}{4r_i} \right) dz = 0 \quad (24)$$

197 Solving the involved product derivatives, applying the Green’s function, and imposing the
198 Neumann-boundary condition, the second equation of Eq. (22), the weak form of the
199 momentum balance equation can be described as

200

$$\begin{aligned} \int_L W \rho_m \frac{\partial u_m}{\partial t} dz + \int_L W u_m \frac{\partial \rho_m}{\partial t} dz - \int_L \rho_m u_m^2 \frac{\partial W}{\partial z} dz - \int_L \gamma \frac{\partial W}{\partial z} dz + W \hat{q}_u |_{r_u} + \int_L W \frac{\partial P}{\partial z} dz \\ + \int_L W \rho_m g \sin\theta dz + \int_L W \frac{f \rho_m |u_m| u_m}{4r_i} dz = 0 \end{aligned}$$

201 Energy balance

$$\int_L W A \left(\frac{\partial}{\partial t} \left[\left(\rho_m h_m + \frac{\rho_m u_m^2}{2} \right) - P \right] + \frac{\partial}{\partial z} \left[\rho_m u_m \left(h_m + \frac{u^2}{2} \right) \right] + \frac{Q}{\pi r_i^2} - \rho_m u_m g \sin\theta \right) dz = 0$$

202

203 Solving the involved product derivatives, applying the Green's function, and imposing the
 204 Neumann-boundary condition, the third equation of Eq. (22), the weak form of the energy
 205 balance equation can be described as

$$\begin{aligned} & \int_L W \rho_m \frac{\partial h_m}{\partial t} dz + \int_L W h_m \frac{\partial \rho_m}{\partial t} dz + \frac{1}{2} \int_L W u_m^2 \frac{\partial \rho_m}{\partial t} dz + \int_L W \rho_m u_m \frac{\partial u}{\partial t} dz - \int_L W \frac{\partial P}{\partial t} dz \\ & + \int_L W \rho_m u_m \frac{\partial h_m}{\partial z} dz + \int_L W h_m \frac{\partial u_m \rho_m}{\partial z} dz - \frac{1}{2} \int_L \rho_m u_m^3 \frac{\partial W}{\partial z} dz + W \hat{q}_e |_{r_e} \\ & + \int_0^L \frac{WQ}{\pi r_i^2} dz - \int_0^L W \rho_m u_m g \sin \theta dz = 0 \end{aligned}$$

206 According to the mass balance equation, Eq. (23), the sum of the second term and seventh
 207 term of the energy balance equation is by definition zero, yielding

$$\begin{aligned} & \int_L W \rho_m \frac{\partial h_m}{\partial t} dz + \frac{1}{2} \int_L W u_m^2 \frac{\partial \rho_m}{\partial t} dz + \int_L W \rho_m u_m \frac{\partial u}{\partial t} dz - \int_L W \frac{\partial P}{\partial t} dz \\ & + \int_L W \rho_m u_m \frac{\partial h_m}{\partial z} dz - \frac{1}{2} \int_L \rho_m u_m^3 \frac{\partial W}{\partial z} dz + W \hat{q}_e |_{r_e} + \int_L \frac{WQ}{\pi r_i^2} dz \quad (25) \\ & - \int_L W \rho_m u_m g \sin \theta dz = 0 \end{aligned}$$

208 The mass density and temperature are important state variables and several other parameters
 209 and states variables are dependent on them. It is therefore necessary to formulate them in
 210 terms of their weighted forms to make them compatible with the primary state variables and
 211 to facilitate the linearization scheme, which is internally conducted by COMSOL.
 212 Applying the weighted residual method to the void fraction equation, Eq. (7), and solving, gives

$$\int_L W' (X \rho_l \rho_m u_m - \alpha C_0 X \rho_l \rho_m u_m - \alpha C_0 (1 - X) \rho_g \rho_m u_m - \alpha \rho_g \rho_l u_{gu}) dz = 0 \quad (26)$$

213 The same can be applied to Eq. (4), giving

$$\int_L W' (\alpha \rho_g + (1 - \alpha) \rho_l - \rho_m) dz = 0 \quad (27)$$

214 Similarly, applying the weighted residual method to the temperature equation, Eq. (11), gives

$$\int_L W' \left(\text{if} \left(P \leq 16.529E6, \text{if} \left(h_m \leq h_l(P, T_s(P)), T_1, \text{if} \left(h_m \leq h_g(P, T_s(P)), T_s, \text{if} \left(P \leq 4E6, T_{2a}, \text{if} \left(h_m \leq h_{2bc}(P), T_{2c}, T_{2b} \right) \right) \right), \text{if} \left(h_m \leq h_l(P, 623.15), T_1, \text{if} \left(h_m \geq h_g(P, T_{B23}(P)), \text{if} \left(h_m \leq h_{2bc}(P), T_{2c}, T_{2b} \right), \text{if} \left(P \leq P_{s3}(h), T_s, T_3 \right) \right) \right) \right) - T \right) dz = 0 \quad (28)$$

215 in which W' is the weighting function, which can be different than that the balance equations.
216 Formulating the constitutive equations by their weighted forms proved to be effective for
217 solving such a problem, which exhibits advection and phase change. Otherwise, the use of the
218 standard linearization of the constitutive equations, which is normally conducted by COMSOL,
219 can cause numerical nuisance and divergence.

220 3.1.1 COMSOL Element technology and solver

221 COMSOL provides a wide range of element types. We utilize the Lagrange test functions for the
222 discretization of the primary state variables. To increase accuracy and decrease oscillations,
223 cubic shape functions are utilized for primary state variables P , u_m and h_m , and quadratic for
224 temperature, mass density and void fraction.
225 The time-dependent fully coupled solver has been employed to solve the finite element
226 equations, and the Backward Differentiation Formula (BDF) has been utilized for the time
227 stepping. The nonlinear systems of equations are solved using a damped Newton method [22].

228 4 Numerical examples and validation

229 Two numerical examples are presented. The first describes the model capability to simulate
230 heat and fluid flow in a geothermal wellbore, which can be connected to a wide range of
231 reservoir enthalpies. The second example focuses on a high enthalpy case, which is utilized to
232 validate the model.

233 4.1 Phase change in low to high enthalpy reservoirs

234 This example presents a numerical simulation of a production wellbore, which can be
235 employed in various types of geothermal reservoirs ranging from low to high enthalpy. The
236 objective of this example is to examine the capability of the computational model for the
237 simulation of the fluid phase change along the wellbore and its association with the reservoir
238 type. Also, it aims at gaining an insight on the physical processes and phenomena occurring
239 along the wellbore and with time.

240 The wellbore geometry and its boundary conditions are shown in Figure 2. The properties of
241 the wellbore and the surrounding formation are given in Table 1.

242 **4.1.1 Initial and boundary conditions**

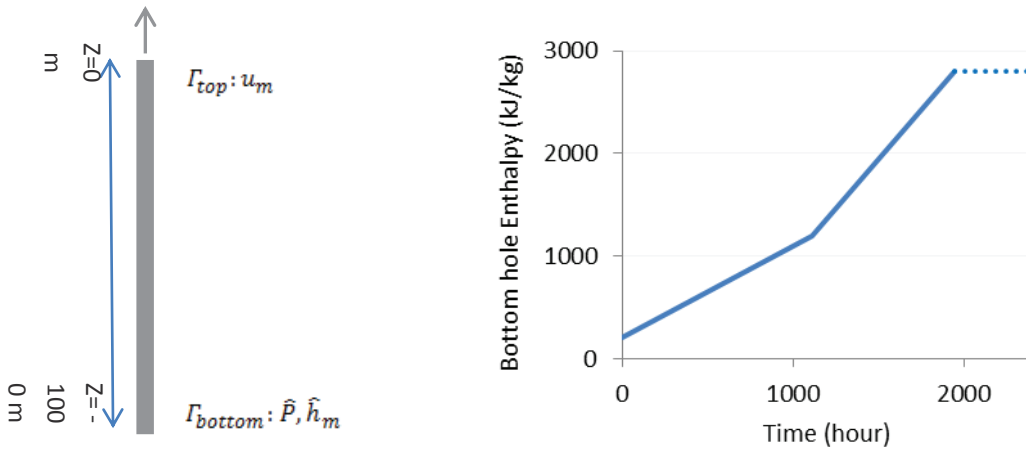
243 Initially, the wellbore is assumed to be filled with liquid water, which is under thermal and
 244 mechanical equilibrium with the atmosphere at the top, low enthalpy reservoir at the bottom
 245 and surrounding rock formation along its length.

246 Due to the hydrostatic pressure and gravity force, and mass density variation with pressure and
 247 enthalpy, the thermal and mechanical equilibrium must be attended before conducting the
 248 transient analysis. For this, we conducted a steady state analysis based on the initial fluid state
 249 and boundary conditions. A constant flow rate with a constant velocity was imposed at the well
 250 head. The computational result of this analysis is utilized as the initial condition for the
 251 transient analysis.

252 **Table 1: Wellbore and formation assumed data**

Inclination Angle	90
Well inner radius (r_i)	0.11 (m)
Casing outer radius (r_o)	0.13 (m)
Length (l)	1000 (m)
Casing thermal conductivity (λ_p)	0.33 ($\text{Wm}^{-1}\text{K}^{-1}$)
Roughness of the wellbore (ε)	1.5E-6 (m)
Surface temperature ($T_{surface}$)	20 °C
Profile parameter (CO) & Drift flux velocity (u_{gu})	Eq. (A 7)

253



254

255 **Figure 2: Geometry and the boundary conditions**

256 The boundary conditions in the transient analysis are:

$$\hat{u}_m = 3 \text{ m/s} \text{ at } z = 0 \text{ m}$$

$$\hat{P} = 10 \text{ MPa} \text{ at } z = -1000 \text{ m}$$

(29)

$$\hat{h}_m = \begin{cases} 0.25t + 2E5 & t \leq 4E6 \text{ s} \\ 0.533t - 9.32E3 & 4E6 \text{ s} < t \leq 7E6 \text{ s} \\ 2.8E6 & t \geq 7E6 \text{ s} \end{cases} \text{ Jkg}^{-1}\text{K}^{-1} \quad \text{at } z = -1000 \text{ m}$$

257 where \hat{h}_m variation with time is plotted in Figure 2.

258 These boundary conditions are chosen to simulate a wide range of geothermal reservoirs,
259 ranging from low to high enthalpy.

260 The temperature of the formation rocks surrounding the wellbore, T_R , appearing in the heat
261 exchange term, Q in Eq. (A 10), is adjusted according to the temperature at the bottom hole,
262 which is a function of pressure and specific enthalpy as given in Eq. (29), as

$$263 \quad T_R = \begin{cases} 293.15 + (T_{bottom} - 293.15) * H/1000 & T \leq 523.15 \text{ K} \\ 293.15 + 0.23 * H & T > 523.15 \text{ K} \end{cases}$$

264 in which T_{bottom} is the bottom hole temperature, calculated at every time step; and H is the
265 wellbore length.

266 4.1.2 Finite element solution and results

267 The weak forms given in Section 3.1 are implemented in COMSOL, and the problem is
268 discretized using linear elements, approximately 20 m in length for each. The physical time for
269 the wellbore production is assumed 2083 hours.

270
271 The computational results along the wellbore and with time for temperature, pressure, vapor
272 volume fraction, vapor mass fraction, mass density and mixture velocity are given in Figure 3.

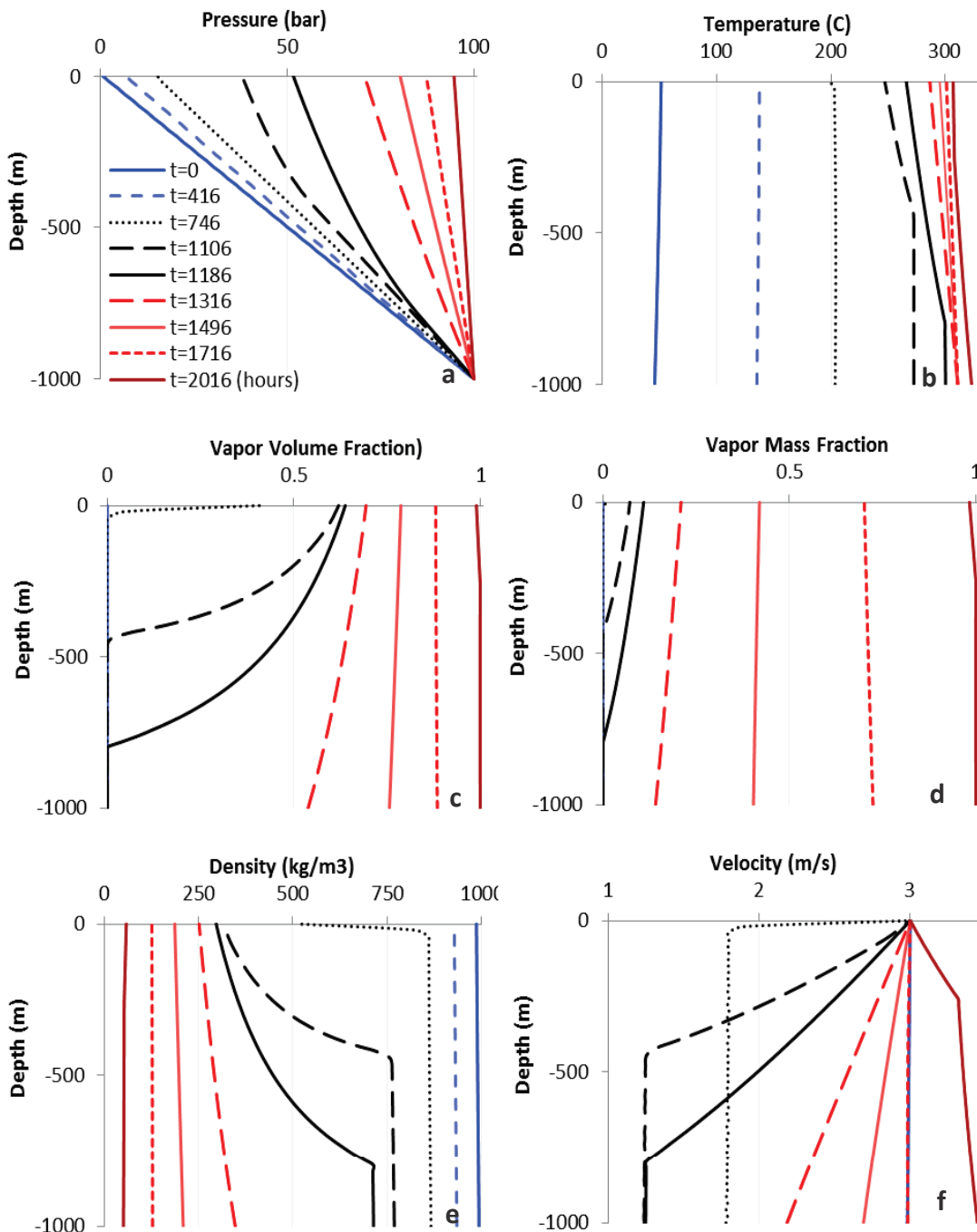
273 Figure 3a shows the pressure distribution along the wellbore at different times. It shows that,
274 initially, the pressure is hydrostatic, but increasing with time due to the thermodynamic effects
275 of varying temperature and density along the wellbore. The wellhead pressure changes from
276 0.6 bar, during the production of hot water at the initial stage, to about 95 bar, during the
277 production of the high temperature vapor at the final stage. As expected, the vapor volume
278 fraction plays an important role in the pressure drop along the wellbore.

279 Figure 3b shows the temperature distribution along the wellbore and with time. The
280 temperature at the bottom varies from 45 °C to about 323°C. By increasing enthalpy, the flash
281 evaporation point moves downwards until reaching to a vapor state at the bottom hole. This is
282 apparent from Figure 3c which shows the vapor volume distribution. As the pressure at the
283 bottom hole is constant and the temperature in the two-phase region is a function of pressure
284 only (Eq.(16)), the bottom hole temperature keeps constant in the period between $t = 1316$
285 hour and $t = 1716$ hour, which is related to the specific enthalpy range between 1592
286 (kJ kg^{-1}) and 2360 (kJ kg^{-1}), and the void fraction between 0.51 and 0.88, respectively.

287 Figure 3c and Figure 3d show the vapor volume fraction and the vapor mass fraction,
288 respectively. They vary between 0 and 1, entailing the variation of fluid state from liquid to
289 mixture to a saturated vapor state.

290 The increase of the vapor content with time is accompanied with the reduction of mass density
291 and increase in velocity, as shown in Figure 3e and Figure 3f, respectively. Velocity logs show an

292 apparently linear trend when only single phase exists along the wellbore, but exhibits a sharp
293 gradient at the flashing or condensation zones. Interesting to observe that, with vaporization
294 (the period between $t = 746$ h and $t = 1186$ h), the fluid runs faster, but with condensation (the
295 period indicated at $t = 2016$ h) the fluid runs slower. This behavior is reflected in the mass
296 density distribution in Figure 3e, but in an inverse sense. At $z = -1000$ m the mass density at the
297 bottom hole changes from 994 kg/m^3 , in the low enthalpy liquid water state, to 51 kg/m^3 , in
298 the saturated vapor state. The transient changes of the mass density and the location of the
299 flash points are in accordance with the variations in the other state variables.
300 Briefly, the computational results, as illustrated in Figure 3, show the computational capability
301 of the proposed model to simulate a wide range of wellbore behaviors exhibiting rigorous
302 phase change.



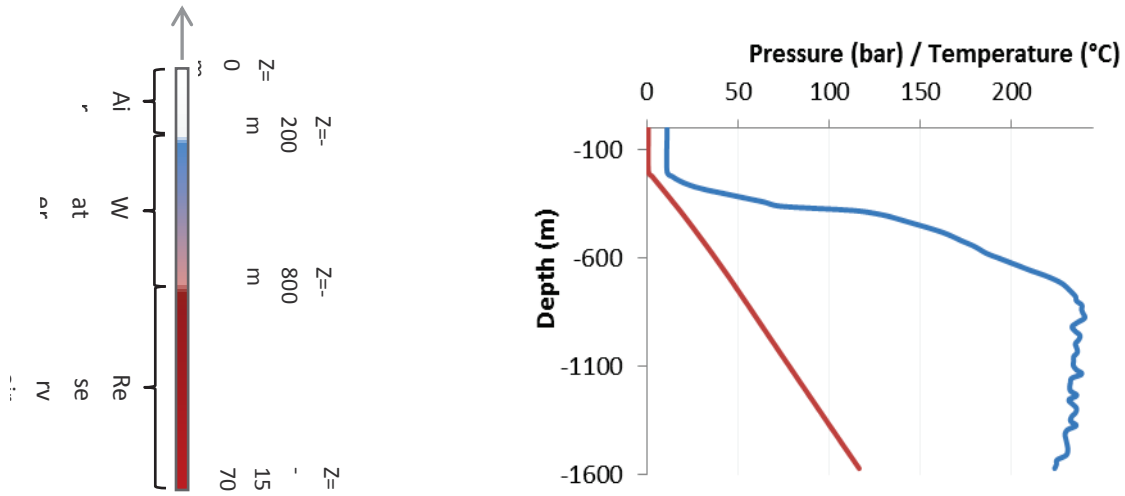
303
304 **Figure 3: Pressure, temperature, vapor volume fraction, vapor mass fraction, density, and velocity**
305 **variations along the well bore for various enthalpy boundary conditions.**

306 **4.2 Experimental validation**

307 The objective of this numerical example is to validate the computational results against field
308 experimental data obtained from a high enthalpy geothermal reservoir.

309 The Sabalan geothermal system, northwest of Iran, is a geothermal reservoir with high-
310 temperature and relatively low pressure. The temperature of Sabalan reservoir is below boiling
311 point, suggesting that it is a liquid-dominated reservoir [23]. This site contains several drilled

312 wellbores, but here we study the behavior of one of them, coined NWS-1. The geometrical and
 313 physical properties of the wellbore are given Table 2. The reservoir starts from depth 800 m,
 314 and the length of wellbore production part is 1570 m, as shown in Figure 4.



328 **Figure 4: Down hole measured stable temperature (Blue log) and pressure (red log) along the NWS-1**
 329 **wellbore; The top 200 meter of well has been filled with air in the natural state.**

330 **Table 2: Geometry and properties of NWS-1 Sabalan**

Inclination Angle	90
Well head elevation	2630 (m)
Well inner radius (r_i)	0.12224 (m)
Casing outer radius (r_o)	0.14224 (m)
Production Part length (L)	1570 (m)
Reservoir depth	800 (m)
Casing thermal conductivity (λ_p)	0.16 ($Wm^{-1}K^{-1}$)
Roughness of the wellbore (ε)	1.5E-6 (m)
Surface temperature ($T_{surface}$)	11 °C
Natural Wellhead pressure (WHP)	0.75 (bar)
The max. flowing WHP	4.5 (bar)
Maximum Measured temperature	240 °C
Profile parameter (CO) & Drift flux velocity (u_{gu})	Eq. (A 8)

331 Initially, the wellbore is filled with water from the well bottom at 1570 m depth to 200 m below
 332 the well head, where above this level, the wellbore is filled with air. The measured temperature
 333 log along the wellbore and in the reservoir is shown in Figure 4. At the surface, the
 334 temperature is on average 11 C and remains nearly the same until 200 m below the surface,
 335 due to the presence of air and its contact with the atmosphere. Below this level, the
 336 temperature increases until reaching around 240 C at 800 m below the surface. The figure also
 337 shows the measured pressure distribution along the wellbore, where in the top 200 m the

338 pressure is atmospheric at 0.77 bar, and below this level, the pressure increases hydrostatically
 339 to reach to around 117 bar at the bottom hole.

340 As the reservoir pressure is not high enough to generate buoyancy forces that can lift the
 341 reservoir water to the ground surface, the NWS-1 wellbore was partly filled with water, and
 342 partly with air. To facilitate discharge from the well, the airlifting technology was conducted
 343 [24]. Airlift is a technology, which aims at reducing the mass density of the initial liquid inside
 344 the wellbore by injecting air that leads the newly formed water-dry air mixture to be less dense
 345 [25].

346 During airlifting, it is reasonable to assume that the mass density of the newly mixed water-dry
 347 air fluid, ρ_{wa} , is homogeneous along the wellbore. Knowing the initial hydrostatic bottom hole
 348 pressure, 117 bar, and the height of the wellbore, 1570 m, the average mass density of the
 349 mixture can then be readily calculated as 758 kg/m³, equivalent to a mixture of 12.7% air and
 350 87.3% water. This assumption of having a homogeneous mass density along the wellbore is of
 351 no significance to the transient computational results during production, but essential to
 352 establish the initial condition.

353 • **Initial and Boundary conditions**

354 Initially, the pressure and temperature along the wellbore, obtained from the field
 355 measurements, are given in Figure 4. The mass density of the water mixture is, as stated above,
 356 758 kg/m³. The specific enthalpy is calculated based on the measured pressure and
 357 temperature, using Eq. (9).

358 Figure 6 shows the initial mixture properties along the wellbore. All other properties including
 359 velocity, vapor volume and vapor mass fraction are set initially to zero.

360 The boundary conditions at the wellhead and well bottom, using Eq. (21) and (22) , are:

361 Wellhead, $z = 0$ m:

$$\Gamma_{WHD}: \hat{u}_m = \frac{\hat{q}(t, z = 0)}{A\rho} \quad (\text{ms}^{-1}) \quad (30)$$

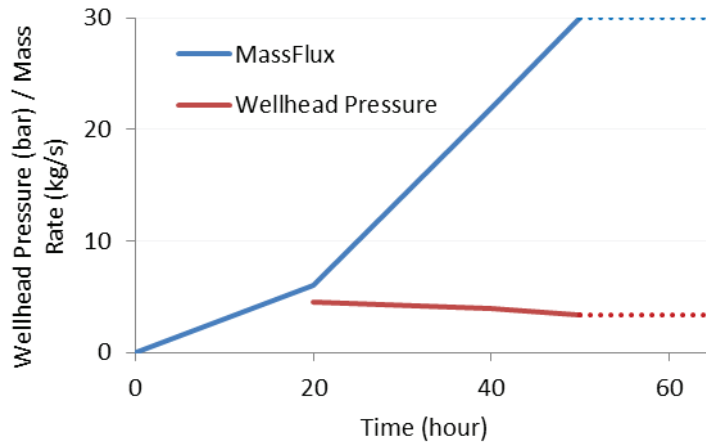
362 Well bottom, $z = -1570$ m:

$$\Gamma_{bottom}: \hat{P} = \begin{cases} 11.7 & t < 72000 \text{ s} \\ \int_{-1570}^0 \rho g dz + \frac{\rho u}{4r_i} \int_{-1570}^0 fu dz + \hat{P}(t, z = 0) & t \geq 72000 \text{ s} \end{cases} \quad (\text{MPa}) \quad (31)$$

$$\hat{h}_m = h_l(\hat{T}, \hat{P}) (\text{J kg}^{-1}) \quad \text{for } \hat{T} = 225 \text{ (}^\circ\text{C)}$$

363 where $\hat{T} = 225 \text{ (}^\circ\text{C)}$ and $\hat{P} = 11.7 \text{ (MPa)}$ are obtained from the measured initial condition,
 364 given in Figure 4 ,and h_l is calculated from Eq. (9). " $\hat{q}(t, z = 0)$ " and " $\hat{P}(t, z = 0)$ " define the
 365 fluid flow rate and pressure at the wellhead, respectively. According to the field data, the
 366 maximum wellhead pressure, at which the wellbore could sustain during production, was 4.5

367 bar; and the mass flow rate was 30 kg/s at 3.4 bar, and 20 kg/s at 4 bar wellhead pressure. The
 368 variations of the wellhead pressure and mass flow rate with time are shown in Figure 5.



369
 370

Figure 5: Wellhead pressure and mass flow rate boundary conditions

371 **4.2.1 Finite element calculation**

372 Using COMSOL, the wellbore is spatially discretized using 78 linear elements, and temporally,
 373 the time is discretized using the backward differentiation formula (BDF).

374 The finite element calculation is conducted in two overlapping steps. In the first step, two fluids
 375 flow is modeled to simulate the airlifting and the start of pumping from the reservoir. In this
 376 step, there exist two fluids exhibiting a jump in thermodynamic properties at the boundary
 377 between them. In the second step, one fluid mixture is modeled to simulate the flow of the
 378 reservoir liquid water-vapor mixture. This process starts upon the end of the airlifting process
 379 and the reach of the reservoir fluid to the wellbore head.

380 **4.2.2 Modeling airlifting**

381 Upon airlifting and start of production, the two mixtures; water-dry air (in the wellbore), and
 382 water-vapor (from the reservoir); travel simultaneously along the wellbore. At the interface
 383 between the two mixtures, the velocity and pressure are continuous, but the mass density and
 384 enthalpy exhibit discontinuity. In finite element analysis, the presence of a discontinuity in the
 385 physical field often causes numerical oscillations. To tackle this problem, we utilize the Level-
 386 Set (LS) method.

387 The LS method is a numerical technique usually utilized to trace a moving interface between
 388 two fluids. Olsson and Kreiss [26] proposed a level set formulation based on a smoothed
 389 Heaviside function, described as

$$\phi = H(\phi_d) = \begin{cases} 0 & \phi_d < -\varepsilon \\ \frac{1}{2} + \frac{\phi_d}{2\varepsilon} + \frac{1}{2\pi} \sin\left(\frac{\pi\phi_d}{\varepsilon}\right) & -\varepsilon \leq \phi_d \leq \varepsilon \\ 1 & \phi_d > \varepsilon \end{cases} \quad (32)$$

390 where $\phi_d = \min(|z - z_{\Gamma_d}|)$ and ε is a transition zone between 0 and 1. The interface
 391 between the two mixtures, Γ_d , is located at $\phi = 0.5$, such that: $\Gamma_d = \{z|\phi(z, t) = 0.5\}$. $\phi = 0$
 392 indicates water-vapor mixture, and $\phi = 1$ indicates water-dry air mixture.

393 The LS function is advected by a field motion equation of the form:

$$\frac{\partial \phi}{\partial t} + u \cdot \nabla \phi = \gamma_{ls} \nabla \cdot \left(\varepsilon \nabla \phi - \phi(1 - \phi) \frac{\nabla \phi}{|\nabla \phi|} \right) \quad (33)$$

394 where u is the drift-flux fluid velocity, and γ_{ls} is a stabilization parameter, chosen here as
 395 0.0001 by trail and error. According to Owkes and Desjardins (2013), if γ_{ls} is too small, ϕ
 396 exhibits oscillations, and if γ_{ls} is too large, the front advects incorrectly. ε depends on the
 397 element size, and chosen to be as small as possible to avoid excessive mass conservation
 398 errors, while maintaining reasonable resolution of the level set function to avoid numerical
 399 difficulties [15].

400 Having located ϕ , the mass density and specific heat capacity, are calculated as

$$\rho = \rho_m + (\rho_{wa} - \rho_m) \cdot \phi \quad (34)$$

401 and

$$C_p = C_{p_m} + (C_{p_{wa}} - C_{p_m}) \cdot \phi \quad (35)$$

402 in which the subscript m indicates formation water-vapor mixture and subscript wa indicates
 403 the airlifted water-dry air mixture. The jump in the material thermal conductivity, viscosity, and
 404 temperature are treated in the same way.

405 4.2.3 Modeling energy production

406 The production process starts from the end of the airlifting until $t = 100$ hours. During this
 407 period, only the reservoir water liquid-vapor mixture exists along the wellbore. The level set
 408 function in this step is zero.

409 4.2.4 Finite element results and discussion

410 Figure 6 shows the computed mixture parameter distributions along the wellbore during
 411 airlifting and production.

412 Figure 6a shows the level set distribution during the airlifting. Initially, before the start of
 413 production, the level set distance parameter reads $\phi = 1$, indicating that the wellbore is filled
 414 with the initial liquid water-dry air fluid, shown in all figures of the Figure 6 by the small dotted
 415 blue line. At the end of airlifting, the level set parameter reads $\phi = 0$, indicating that the
 416 wellbore is filled with the reservoir water liquid-vapor fluid, shown in the figure by the solid red
 417 line. For $0 < \phi < 1$, the level set parameter denotes the location of the interface between the
 418 two fluids along the wellbore. The figure shows a smooth transition between the two mixtures,
 419 as prescribed by Eq. (34). The air lifting process takes 10 hours, after which the reservoir water
 420 reaches to the well head.

421 Figure 6b, shows the pressure distribution along the wellbore. The dotted blue lines show the
 18

422 pressure distribution during the airlifting. The figure shows that, at the beginning, the bottom
423 hole pressure is fixed at 117 bars, prescribed in Eq. (31), and the reduction along the wellbore
424 is hydrostatic. After 20 hours of production, the pressure at the bottom hole becomes a
425 function of the wellhead pressure, friction and hydrostatic pressure, which is significantly
426 affected by the increase in vapor content.

427 The increase in vapor volume and mass fractions are shown in Figure 6c and 7d. These figures
428 show a significant increase in the vapor contents at the flash evaporation locations along the
429 wellbore. The flash evaporation occurs due to reduction of pressure, accompanied by a certain
430 range of high temperature.

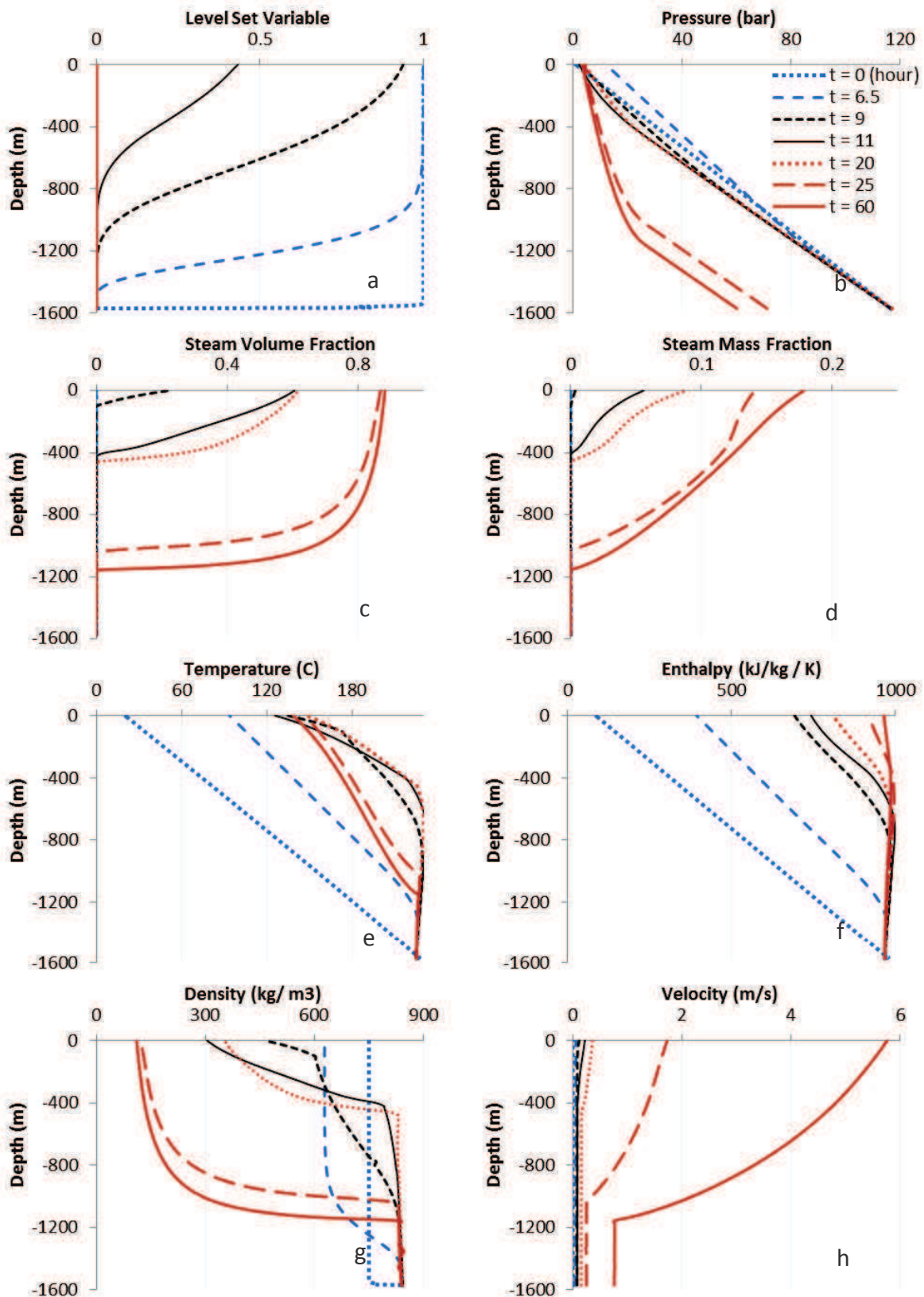
431 Figure 6e shows the temperature distribution along the wellbore. The temperature at the
432 bottom is 225°C, assumed equal to the reservoir temperature. The well head temperature
433 varies from initially 11 °C to about 140 °C after 50 hours of production and stays constant till
434 100 hours. The temperature log shows the flash points, where there is a sharp decrease in
435 temperature in the downstream as compare to that at the upstream, due latent heat
436 vaporization. The locations of these flash points are consistent in all other property
437 distributions.

438 Figure 6f shows the specific enthalpy distribution along the wellbore. With increasing the mass
439 flow rate, the specific enthalpy exhibits little variation. For a 30 kg/s flow rate, the computed
440 wellhead specific enthalpy is 965 ($kJ\ kg^{-1}$), similar to that at the bottom hole. The bottom
441 hole enthalpy is computed as a function of the bottom hole pressure and temperature, using
442 Eq. (31), but yet it can be assumed constant because the variation is too small, ranging
443 between 969 and 967 ($kJ\ kg^{-1}$).

444 Figure 6g shows the distribution of mass density along the wellbore. As expected, the mixture
445 density starts to drop at the flash point, in contrary to the vapor content. After 50 hours of
446 production, it reaches to a minimum value of 110 kg/m³ at the wellhead, related to about 88%
447 vapor volume fraction.

448 Figure 6h shows the velocity distribution along the wellbore. The increase of velocity with time
449 is in consistence with the increase of the flow rate, given in Figure 5. The figure shows that, at
450 the flash points, the velocity exhibits a sharp increase.

451 At the end of production, after 100 hours, the vapor volume fraction at the wellhead is 0.88
452 and the mass fraction is 0.18. The wellhead pressure is 3.4 bar, related to the maximum flow
453 rate of 30 kg/s. these information could be efficiently used for separator designing and power
454 generating.



455

456

Figure 6: simulated properties of fluid during the flowing time along the wellbore

457 **4.2.5 Comparison to measured data**

458 The computational results are compared to the available measured data from the field, taken
 459 at the wellhead and along the wellbore. Figure 7 shows the computed and measured pressure
 460 and temperature distributions for the maximum flow rate of 30 kg/s, at t = 100 hours. Table 3
 461 and Table 4 show detailed comparison at the wellhead and along the wellbore.

462 Apparently, there is a good agreement between the computed results and the measured data.
 463 However, the computed temperature at the wellhead is 139 C, while the measured one is 150
 464 C. This can be attributed to the changes in the surface air temperature, which, in the model,
 465 considered constant. The computed flashing depth is 1136 m, while the measured is around
 466 1170 m. Even though this difference is not significant compared to the wellbore length, the
 467 difference can be attributed to that not all initial and boundary conditions are measured, and in
 468 the model we ought to back calculate them to infer the field conditions, which most likely not
 469 exact.

470 **Table 3: Simulation results versus measured data at the wellhead**

471

	Pressure (bar)	Total flow rate (kg/s)	Steam mass rate (kg/s)	Enthalpy (kJ/kg/ K)
Measured	4.00	22	3.68	950 - 1000
Simulated	Prescribed BC	Prescribed BC	3.61	956.88
Measured	3.4	30	5.5	950 - 1000
Simulated	Prescribed BC	Prescribed BC	5.4	965

472

473 **Table 4: Simulation results versus measured data along the wellbore**

474

	Bottom hole flowing Pressure (bar)	Flashing depth (m)	Wellhead temperature (C)	Flashing point temperature (C)
Measured	60.09	1170	150	223
Simulated	60.17	1136	139	223

475

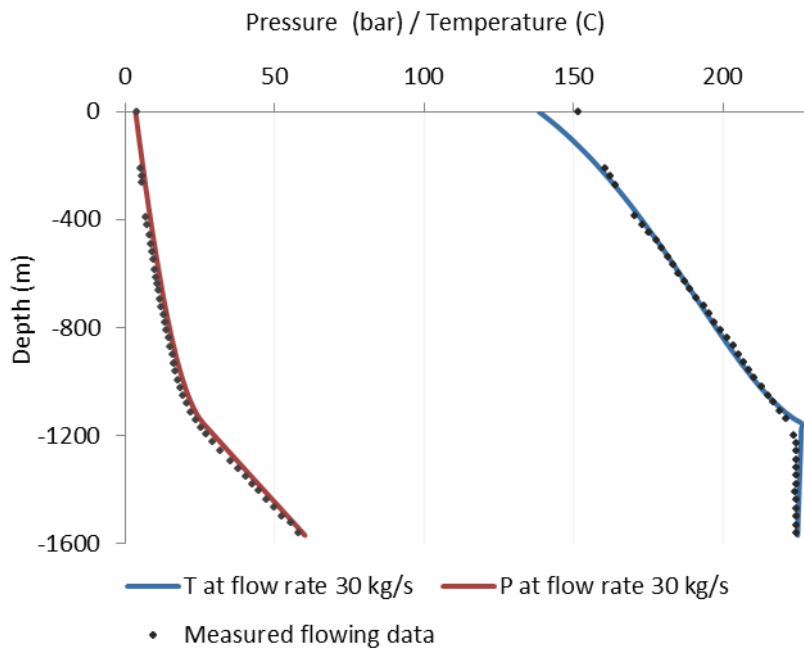


Figure 7: Simulation results versus measured data along the wellbore

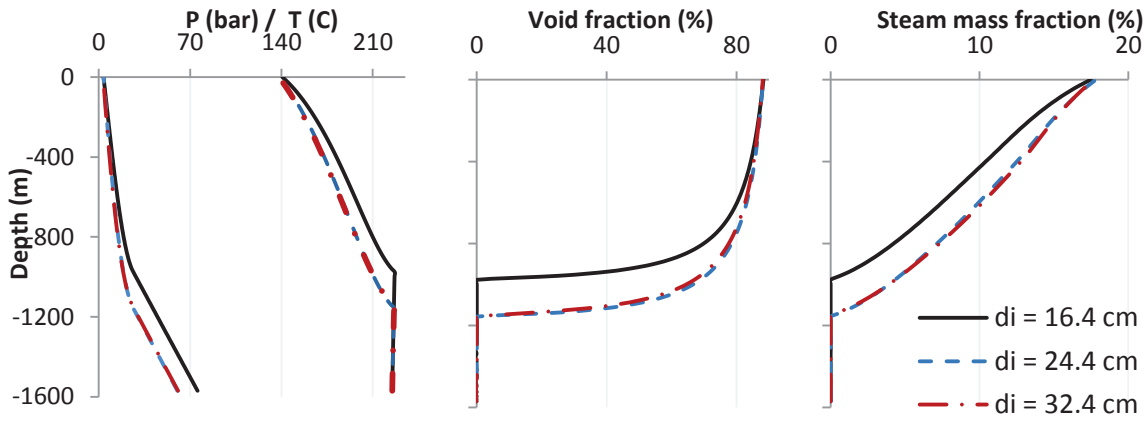
476
477

478 4.3 Parametric analysis

479 Three parametric analyses have been conducted to study the effects of: (i) wellbore diameter,
480 (ii) wellbore wall roughness, and (iii) drift flux profile parameter. The first two parameters are
481 physical, and normally utilized for wellbore design, and the third is numerical, and employed
482 for the evaluation of the drift flux constitutive models. The geometry and material parameters,
483 except for the examined parameters, utilized in this analysis are similar to those adopted in the
484 numerical example given in Section 4.2 .

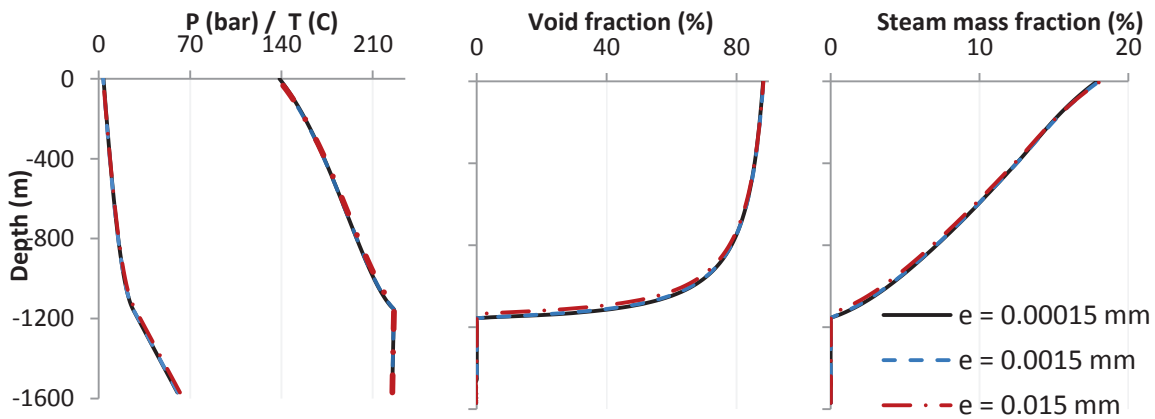
- 485 1. **Wellbore diameter:** Three wellbore diameters are examined: 16.4 cm, 24.4 cm and 32.4
486 cm. Figure 9 shows the computational results of pressure, temperature, void fraction and
487 steam mass fraction distributions along the wellbore for the three cases. It illustrates that
488 by increasing the wellbore diameter from 16.4 cm to 24.4 cm, the flashing zone depth
489 moves from 970 m to 1170 m, and at the wellbore bottom-hole, the pressure decreased
490 from 75 bar to 60 bar. However, the increase of the wellbore diameter from 24.4 cm to
491 32.4 cm exhibits no significant effect. The void fractions, steam fraction, pressure and
492 temperature at the wellhead are nearly the same for the three cases.
- 493 2. **Wellbore wall roughness:** Three friction coefficients are examined: 0.015 mm, 0.0015 mm
494 and 0.00015 mm. Figure 9 shows the computational results of pressure, temperature, void
495 fraction and steam mass fraction distributions along the wellbore for the three cases. It
496 illustrates that, for the studied cases, the wellbore wall roughness has no significant effect
497 on the fluid flow.
- 498 3. **Drift flux profile parameter:** Three constitutive equations, Eqs. A6, A7 and A8 given in Table
499 A1, describing the drift flux profile parameter, C_0 , and its associated drift flux velocity, u_{gw} ,
500 are examined. Figure 10 shows the computational results of pressure, temperature, void

501 fraction and steam mass fraction distributions along the wellbore for the three cases. It
 502 demonstrates that Eq. A6 and Eq. A8 produce reasonably similar computational results
 503 along the wellbore, but Eq. A7 exhibits deviation from both, though with similar trend.
 504 Following our verification example given in Section 4.2, it seems that Eq. A8 has produced
 505 the best fit, followed by Eq. A6.
 506



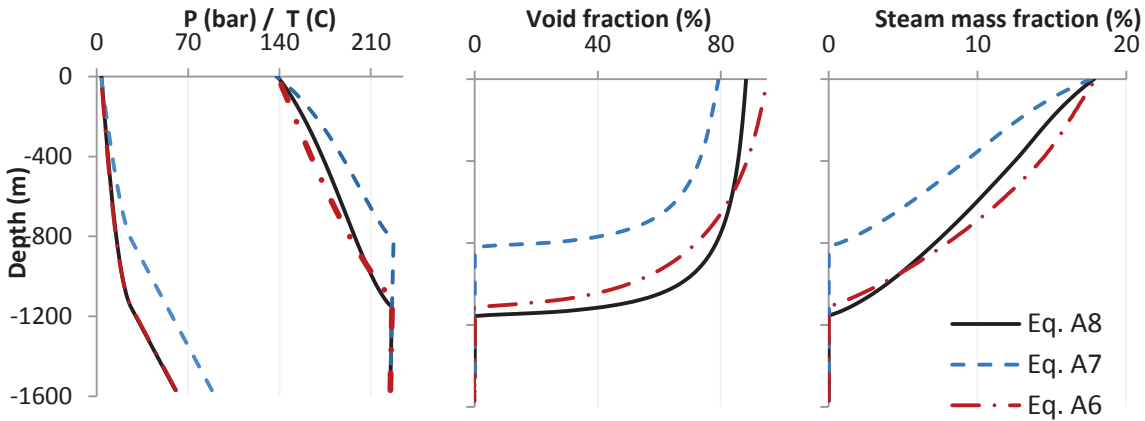
507
 508 **Figure 8: Effect of well diameter, at t = 60 hour**
 509

510



511
 512 **Figure 9: Effect of wellbore roughness, at t = 60 hour**
 513

514



515
516 **Figure 10: Effect of different constitutive models for the drift flux profile parameter, at t = 60 hour**
517

518 **5 Conclusion**

519 In high enthalpy geothermal systems, predicting the fluid properties along the wellbore, such
520 as temperature, phase composition and mass density is vital for their design and monitoring.
521 The fluid along the wellbore exhibits phase change, which is manifested by the occurrence of
522 flash evaporation, arising from pressure reduction, accompanied by a certain range of
523 temperatures. Below and above the flash point, the fluid exhibits sudden change in material
524 composition, which can cause a significant change in its properties and behavior. Such kind of
525 physical behavior is computationally challenging and demanding. Solving this kind of problems
526 constitutes the focal point of the presented work.

527 The conceptual model and the mathematical formulation are designed to simulate a wide
528 range of enthalpies and initial and boundary conditions. All important physical phenomena and
529 processes occurring along the wellbore, including buoyancy, phase change, compressibility,
530 thermal interaction, wall friction and slip between phases are considered. They are also
531 designed to simulate airlifting of water and air, which initially exist in the wellbore before
532 production. The airlifting inevitably gives rise to the existence of two fluids along the wellbore:
533 airlifted water-dry air fluid, and reservoir water-vapor fluid. At the boundary between the two
534 fluids there is a discontinuity in the thermodynamic properties. The discontinuity is modeled
535 using the level-set method, which is coupled to the drift-flux model via the fluid velocity.

536 The numerical model is designed to solve the governing equations using the finite element
537 method. The finite element package, COMSOL Multiphysics, is utilized as a framework for
538 implementing and discretizing the governing equations. These equations are dynamic,
539 advective, nonlinear and involve phase change, together with buoyancy, friction, slip forces and
540 discontinuity at the boundary between two fluids. Solving such a problem using standard
541 strong form implementation is not possible, unless excessively fine meshes and small time
542 steps are utilized. Yet, the calculation can be unstable and non-convergent. Instead, we solved
543 this problem by implementing the weak forms of the governing equations, using the weighted

544 residual finite element method.

545 The computational capability of the model has been tested by solving two numerical examples
546 with different initial and boundary conditions. The computational results clearly exhibit the
547 occurrence of phase change along the wellbore, the extent of which depends on the enthalpy
548 of the reservoir. The accuracy of the model is examined by comparing its results with those
549 obtained from field data.

550 The parametric analyses have shown that the model can be readily utilized for engineering
551 design of geothermal wellbores. We show that the increase of wellbore diameter can change
552 the fluid state profile along the wellbore, but to a certain limit, after which, the increase of
553 diameter will not have a significant effect. We also show that the wall roughness has, for the
554 studied range, no significant effect.

555 The paper shows that, despite the complexity of the involved physical phenomena, it is possible
556 to model such a problem using commercial packages, supporting user programming interface, as
557 a framework for discretization. However, an innovative implementation of the governing
558 equations is necessary, and requires an in depth knowledge on the mathematical formulation,
559 numerical discretization and software features.

560 **Appendix A. Model Parameters**

561 The wellbore wall friction coefficient, f , in Eq. (2), can be described as [11]:

$$f = \begin{cases} \frac{16}{Re} & Re \leq 2400 \\ \frac{1}{16} \left\{ \log \left[\frac{\xi}{3.7r_i} - \frac{5.02}{Re} \log \left(\frac{\xi}{3.7r_i} + \frac{13}{Re} \right) \right] \right\}^{-2} & Re \geq 2400 \end{cases} \quad (\text{A } 1)$$

562

563 where ξ is the roughness of the wellbore, assumed 0.0015 mm, and Re is the Reynolds number
564 given by:

$$Re = \frac{\rho_m |u_m| (2r_i)}{\mu_m} \quad (\text{A } 2)$$

565 in which μ_m is the dynamic viscosity, described in Eq. (A 12).

566 The slip parameter between two phases, γ , in the momentum balance equation, could be
567 defined as [12]:

$$\gamma = \frac{\alpha \rho_g \rho_l \rho_m}{(1 - \alpha) \rho_m^*} [(C_0 - 1)u_m + u_{gu}]^2 \quad (\text{A } 3)$$

568 where α is the gas volume fraction, ρ_g is the gas density and ρ_l is the liquid density, and ρ_m^*
569 defines the profile-adjusted average density, described as:

$$\rho_m^* = \alpha C_0 \rho_g + (1 - \alpha C_0) \rho_l \quad (\text{A } 4)$$

570 u_{gu} and C_0 are the drift flux velocity and profile parameter, respectively. Table A 1 gives

571 various definitions, with their corresponding literature. Here we utilize Eq. (A 7) and (A 8) in
 572 example 1 and 2, respectively.

573 σ_{gl} is the surface tension, valid over the vapor-liquid saturation line for the temperature range
 574 between 0 and 373.946 °C [21]. It is described as

$$\sigma_{gl} = 0.2358 \left(1 - \frac{T}{647.096}\right)^{1.256} \left[1 - 0.625 \left(1 - \frac{T}{647.096}\right)\right] \quad (\text{A } 5)$$

575 **Table A 1: Various expressions for C_0 and u_d**

Expression	Eq. Number	Reference
$C_0 = \frac{C_{max}}{1 + (C_{max} - 1)\eta^2}$ $\eta = \frac{\beta - B}{1 - B}$ $B = \frac{2}{C_{max}} - 1.0667$ $\beta = \max\left(\alpha_2, F_V \frac{\alpha_2 u_m }{u_{sgf}}\right), 0 \leq \beta \leq 1$ $u_{sgf} = K_u \left(\frac{\rho_1}{\rho_2}\right)^{0.5} \left[\frac{g\sigma_{gl}(\rho_l - \rho_g)}{\rho_l^2}\right]^{1/4}$ $K_u = \left[\frac{142}{\sqrt{N_B}} \left(\sqrt{1 + \frac{N_B}{161.312}} - 1\right)\right]^{0.5}$ $N_B = 4r_i^2 \left[\frac{g(\rho_l - \rho_g)}{\sigma_{gl}}\right]$ <p>where C_{max} is assumed 1.1, η is a parameter reflecting the effect of the flow status on the profile parameter, $F_V = 1$, K_u is the Kutateladze number, and N_B is the Bond number.</p> $u_{gu} = \frac{1.85(1 - \alpha C_0)K \left[\frac{g\sigma_{gl}(\rho_l - \rho_g)}{\rho_l^2}\right]^{1/4}}{\alpha C_0 \sqrt{\frac{\rho_g}{\rho_l}} + 1 - \alpha C_0} \quad \text{for a vertical wellbore}$ <p>K is a smooth transition function defined as:</p> $K = \begin{cases} 1.53 & \alpha \leq 0.06 \\ 1.53 + \frac{C_0 K_u - 1.53}{2} \left[1 - \cos\left(\pi \frac{\alpha - 0.06}{0.15}\right)\right] & 0.06 \leq \alpha \leq 0.21 \\ C_0 K_u & \alpha \geq 0.21 \end{cases}$	(A 6)	[11, 13]

$C_0 = 1 + 0.2(1 - X) \left(\frac{gd_i \rho_l^2}{m^2} \right)^{0.25}$ <p>for $\alpha \geq 0.1$ m is the mass velocity.</p>	$u_{gu} = 1.18 (1 - X) \left[\frac{g\sigma_{gl}(\rho_l - \rho_g)}{\rho_l^2} \right]^{1/4}$	(A 7)	[19, 20]
$C_0 = 1 + 0.2(1 - X) \quad \text{for } \alpha < 0.1$			
$C_0 = 1.1 \quad \text{for } m \geq 200$ $C_0 = 1.54 \quad \text{for } m < 200$ <p>m is the mass velocity</p>	$u_{gu} = 1.18 \left[\frac{g\sigma_{gl}(\rho_l - \rho_g)}{\rho_l^2} \right]^{1/4}$	(A 8)	[19, 20]
$C_0 = 1.2$	$u_{gu} = 1.53 \left[\frac{g\sigma_{gl}(\rho_l - \rho_g)}{\rho_l^2} \right]^{1/4}$	(A 9)	[2]

576 Q in Eq. (3) describes the heat exchange between the wellbore wall and its surrounding
577 formation, defined as [11]:

$$Q(z) = 2\pi r_w U(T - T_R(z)) \quad (\text{A 10})$$

$$U = \frac{1}{R_{conv} + R_{cond}}$$

$$R_{conv} = r_0 / (r_w \bar{h})$$

$$R_{cond} = r_0 \ln(r_0 / r_w) / \lambda_p$$

$$\bar{h} = \text{Nu} \lambda_m / (2r_i)$$

$$\text{Nu} = \begin{cases} 0.665 Re^{1/2} Pr^{1/3}, & Re < 2000 \\ 0.023 Re^{0.8} Pr^{0.4}, & Re \geq 2000 \end{cases}$$

$$\text{Pr} = \frac{\mu_m c_{pm}}{\lambda_m}$$

578 where $T_R(z)$ is the temperature of the surrounding formation, in contact with the formation,
579 and U is the thermal interaction coefficient of wellbore, with R_{conv} and R_{cond} are the thermal
580 resistance of the fluid and casing material, respectively. r_w is the outer radius of the casing, r_0
581 is the outer radius of the wellbore, λ_p is the thermal conductivity of the casing material, and \bar{h} is
582 the convective heat transfer coefficient, with Nu the Nusselt number and Pr the Prandtl
583 number. c_{pm} , μ_m and λ_m are the specific heat capacity, dynamic viscosity and thermal
584 conductivity of the mixture described in Eqs.(A 11), (A 12) and (A 13), respectively.

585 The specific isobaric heat capacity is defined in terms the specific heat capacity of the liquid
586 phase and the gas phase, and their volume fractions, as

$$C_{p_m}(P, T) = -\alpha \left(\frac{\partial h_g}{\partial T} \right)_P - (1 - \alpha) \left(\frac{\partial h_l}{\partial T} \right)_P \quad (\text{A 11})$$

587 in which h_g and h_l are specific enthalpies of vapor and liquid phases, described in Eqs. (9) and (

588 10), respectively.

589 Considering the effects of density and temperature, the dynamic viscosity, μ_m , and the mixture
590 thermal conductivity, λ_m , can be described as

$$\mu_m(\rho, T) = 10^{-6} \left(\frac{T}{647.096} \right)^{0.5} \left[\sum_{i=1}^4 n_i^o \left(\frac{T}{647.096} \right)^{1-i} \right]^{-1} \exp \left[\sigma_{gl} \sum_{i=1}^{21} n_i \left(\frac{\rho_m}{322} - 1 \right)^{I_i} \left(\left(\frac{T}{647.096} \right)^{-1} - 1 \right)^{J_i} \right] \quad (\text{A } 12)$$

591

$$\lambda_m(\rho, T) = \left(\frac{T}{647.26} \right)^{0.5} \sum_{i=1}^4 n_i^o \left(\frac{T}{647.26} \right)^{i-1} + n_1 + n_2 \frac{\rho_m}{317.17} + n_3 \exp \left[n_4 \left(\frac{\rho_m}{317.17} + n_5 \right)^2 \right] + \left(n_1 \left(\frac{T}{647.26} \right)^{-10} + n_2 \right) \left(\frac{\rho_m}{317.17} \right)^{1.8} \exp \left[n_3 \left(1 - \left(\frac{\rho_m}{317.17} \right)^{2.8} \right) \right] + n_4 A \left(\frac{\rho_m}{317.17} \right)^B \exp \left[\left(\frac{B}{1+B} \right) \left(1 - \left(\frac{\rho_m}{317.17} \right)^{1+B} \right) \right] \quad (\text{A } 13)$$

where

$$A = 2 + n_8 \left(\left| \frac{T}{647.26} - 1 \right| + n_{10} \right)^{-0.6}$$

$$B = n_9 \left(\left| \frac{T}{647.26} - 1 \right| + n_{10} \right)^{-0.6} \quad \text{for } T < 647.26$$

592 where the n_i coefficients are constant values, which can be found in IAPWS-IF97.

593 **Appendix B. IAPWS formulation of water and steam**

594 The temperatures of geothermal resources for most known fields range from about 50 °C, in
595 low enthalpy fields, to about 160 – 280 °C, in relatively high enthalpy fields. According to Figure
596 1, this range of temperatures is included in regions 1, 2 and 4, which are related to liquid, gas
597 and two-phase mixture, respectively.

598 The specific Gibbs free energy, g_1 and g_2 , for single-phase fluid, which falls in region 1 or 2 can
599 be described respectively as

$$g_1(P, T) = R T \sum_{i=1}^{34} n_i \left(7.1 - \frac{P}{16.53\text{E}6} \right)^{I_i} \left(\frac{1386}{T} - 1.222 \right)^{J_i} \quad (\text{B } 1)$$

$$g_2(P, T) = R T \ln \left(\frac{P}{1E6} \right) \sum_{i=1}^9 n_i^o \left(\frac{540}{T} \right)^{J_i^o} \quad (B 2)$$

$$+ R T \sum_{i=1}^{43} n_i \left(\frac{P}{1E6} \right)^{I_i} \left(\frac{540}{T} - 0.5 \right)^{J_i}$$

600 where $R = 461.526 \text{ Jkg}^{-1}\text{K}^{-1}$.

601 For a vapor mass fraction of more than 95%, $g_2(P, T)$ is replaced by what is known as the
 602 metastable vapor equation, which is only different from Eq. (B 2) by its coefficients [21]. For
 603 region 4, however, the saturation liquid properties are calculated by Eqs. (B 1) of region 1, and
 604 the saturation vapor properties are calculated by Eqs. (B 2) of region 2.

605 The coefficient $n_i, n_i^o, n_i', I_i, J_i, J_i^o$ can be found in IAPWS-IF97 [21]. They have different values
 606 in different equations.

607 References

- 608 1. Poettmann, F.H. and P.G. Carpenter, *Multiphase Flow of Gas, Oil and Water through*
 609 *Vertical Strings with Application to the Design of Gas Lift Installation*, in *API*
 610 *(American Petroleum Institute) Drilling and Production Practice*. 1952: Midland.
 611 Texas. p. 257-317.
- 612 2. Zuber, N. and J.A. Findlay, *Average Volumetric Concentration in Two-Phase Flow*
 613 *Systems*. *Journal of Heat Transfer*, 1965. **87**: p. 453-468.
- 614 3. Gould, T.L., *Vertical Two-Phase Steam-Water Flow in Geothermal Wells*. *Journal of*
 615 *Petroleum Technology*, 1974. **26**: p. 833-842.
- 616 4. Goyal, K.P., C.W. Miller, and M.J. Lippmann. *Effect of Wellhead Parameters and Well*
 617 *Scaling on the Computed Downhole Conditions in Cerro Prieto Wells*. in *The 6th*
 618 *Workshop on Geothermal Reservoir Engineering* 1980. Stanford University, Stanford,
 619 California, USA.
- 620 5. Miller, C.W., *Wellbore User's Manual*. 1980, Berkeley, University of California.
- 621 6. Aunzo, Z.P., G. Bjornsson, and G.S. Bodvarsson, *Wellbore Models GWELL, GWNACL,*
 622 *and HOLA User's Guide*. 1991: Berkeley, University of California, USA
- 623 7. Bjornsson, G. and G.S. Bodvarsson, *A Multi-feed zone geothermal wellbore simulator*. .
 624 *Geothermal Resources Council Transactions*, 1987. **11**: p. 503–507.
- 625 8. Gudmundsdottir, H., M. Thor Jonsson, and H. Palsson. *THE WELLBORE SIMULATOR*
 626 *FLOWELL*. in *Thirty-Eighth Workshop on Geothermal Reservoir Engineering*. 2013.
 627 Stanford University, Stanford, California.
- 628 9. Saeid, S., R. Al-Khoury, and F. Barends, *An efficient computational model for deep*
 629 *low-enthalpy geothermal systems*. *Computers & Geosciences*, 2013. **51**: p. 400-409.
- 630 10. Kaya, A.S., C. Sarica, and J.P. Brill. *Comprehensive Mechanistic Modeling of Two-Phase*
 631 *Flow in Deviated Wells*. in *Society of Petroleum Engineers Annual Technical*
 632 *Conference*. 1999. Houston, Texas.
- 633 11. Mousivand Arzanfudi, M. and R. Al-Khoury, *A compressible two-fluid multiphase*
 634 *model for CO2 leakage through a wellbore*. *International Journal for Numerical*
 635 *Methods in Fluids*, 2015. **77**(8): p. 477–507.

- 636 12. Pan, L.H., S.W. Webb, and C.M. Oldenburg, *Analytical solution for two-phase flow in a*
637 *wellbore using the drift-flux model*. *Advances in Water Resources*, 2011. **34**(12): p.
638 1656-1665.
- 639 13. Shi, H., Holmes, J. A., Durlafsky, L. J., Aziz, K., Diaz, L., Alkaya, B., & Oddie, G. , *Drift-*
640 *Flux Modeling of Two-Phase Flow in Wellbores*. Society of Petroleum Engineers,
641 2005.
- 642 14. Faghri, A. and Y. Zhang, *Transport Phenomena in Multiphase Systems*. 2006, USA:
643 Elsevier.
- 644 15. Owkes, M. and O. Desjardins, *A discontinuous Galerkin conservative level set scheme*
645 *for interface capturing in multiphase flows*. *Journal of Computational Physics*, 2013.
646 **249**: p. 275-302.
- 647 16. Sethian, J.A. and P. Smereka, *Level Set Methods for Fluid Interfaces*. *Annual Review of*
648 *Fluid Mechanics*, 2003. **35**(35): p. 341-372.
- 649 17. Lewis, K.C. and R.P. Lowell, *Numerical modelling of two-phase flow in NaCl-H₂O flow*
650 *in the NaCl-H₂O system: Introduction of a numerical method and benchmarking*.
651 *Journal of Geophysical research*, 2009. **114**: p. 1-18.
- 652 18. Palliser, C.C. and R. McKibbin, *A Model for Deep Geothermal Brines,III:*
653 *Thermodynamic Properties – Enthalpy and Viscosity*. *Transport in Porous Media*
654 1998. **33**(1): p. 155-171.
- 655 19. Rouhani, S. and E. Axelsson, *Calculation of Void Volume Fraction in the Subcooled and*
656 *Quality Boiling Regions*. *Journal of Heat and Mass Transfer*, 1970. **13**(2): p. 383-393.
- 657 20. Thome, j.r., *Chapter 17:Void fraction in two phase flows, in engineering data book III*.
658 2004, Wolverine Tube, Inc.
- 659 21. Wagner, W. and H.J. Kretzschmar, *International Steam Tables - Properties of Water*
660 *and Steam Based on the Industrial Formulation IAPWS-IF97*. 2008: Springer-Verlag
661 (Berlin).
- 662 22. Süli, E. and D. Mayers, *An Introduction to Numerical Analysis*. 2003: Cambridge
663 University Press.
- 664 23. Porkhial, S., et al. *Interpretation of the Injection and Heat Up tests at Sabalan*
665 *geothermal field, Iran*. in *World Geothermal Congress 2015*. 2015. Melbourne,
666 Australia.
- 667 24. Rahmani, M.R., *Assesment of calcite scaling potential in the geothermal wells of the*
668 *NW-Sabalan geothermal prospect, NW-Iran*. 2007, GEOTHERMAL TRAINING
669 PROGRAMME, Iceland: report for SUNA (Renewable Energy Organization of Iran).
- 670 25. Grant, M.A. and P.F. Bixley, *Chapter 8: Production Testing, in Geothermal Reservoir*
671 *Engineering*. 2011, Elsevier Inc.
- 672 26. Olsson, E. and G. Kreiss, *A conservative level set method for two phase flow*. *Journal of*
673 *Computational Physics*, 2005. **210**: p. 225-246.
- 674

Table 1: Wellbore and formation assumed data

Inclination Angle	90
Well inner radius (r_i)	0.11 (m)
Casing outer radius (r_o)	0.13 (m)
Length (l)	1000 (m)
Casing thermal conductivity (λ_p)	0.33 ($\text{Wm}^{-1}\text{K}^{-1}$)
Roughness of the wellbore (ε)	1.5E-6 (m)
Surface temperature ($T_{surface}$)	20 °C
Profile parameter (CO) & Drift flux velocity (u_{gu})	Eq. Error! Reference source not found.

Table 2: Geometry and properties of NWS-1 Sabalan

Inclination Angle	90
Well head elevation	2630 (m)
Well inner radius (r_i)	0.12224 (m)
Casing outer radius (r_o)	0.14224 (m)
Production Part length (L)	1570 (m)
Reservoir depth	800 (m)
Casing thermal conductivity (λ_p)	0.16 ($\text{Wm}^{-1}\text{K}^{-1}$)
Roughness of the wellbore (ε)	1.5E-6 (m)
Surface temperature ($T_{surface}$)	11 °C
Natural Wellhead pressure (WHP)	0.75 (bar)
The max. flowing WHP	4.5 (bar)
Maximum Measured temperature	240 °C
Profile parameter (CO) & Drift flux velocity (u_{gu})	Eq. Error! Reference source not found.

Table 3: Simulation results versus measured data at the wellhead

	Pressure (bar)	Total flow rate (kg/s)	Steam mass rate (kg/s)	Enthalpy (kJ/kg/K)
Measured	4.00	22	3.68	950 - 1000
Simulated	Prescribed BC	Prescribed BC	3.61	956.88
Measured	3.4	30	5.5	950 - 1000
Simulated	Prescribed BC	Prescribed BC	5.4	965

Table 4: Simulation results versus measured data along the wellbore

	Bottom hole flowing Pressure (bar)	Flashing depth (m)	Wellhead temperature (C)	Flashing point temperature (C)
Measured	60.09	1170	150	223
Simulated	60.17	1136	139	223

Table A 1: Various expressions for C_0 and u_d

Expression	Eq. Number	Reference
------------	---------------	-----------

$C_0 = \frac{C_{max}}{1 + (C_{max} - 1)\eta^2}$ $\eta = \frac{\beta - B}{1 - B}$ $B = \frac{2}{C_{max}} - 1.0667$ $\beta = \max\left(\alpha_2, F_V \frac{\alpha_2 u_m }{u_{sgf}}\right), 0 \leq \beta \leq 1$ $u_{sgf} = K_u \left(\frac{\rho_1}{\rho_2}\right)^{0.5} \left[\frac{g\sigma_{gl}(\rho_l - \rho_g)}{\rho_l^2}\right]^{1/4}$ $K_u = \left[\frac{142}{\sqrt{N_B}} \left(\sqrt{1 + \frac{N_B}{161.312}} - 1\right)\right]^{0.5}$ $N_B = 4r_i^2 \left[\frac{g(\rho_l - \rho_g)}{\sigma_{gl}}\right]$ <p>where C_{max} is assumed 1.1, η is a parameter reflecting the effect of the flow status on the profile parameter, $F_V = 1$, K_u is the Kutateladze number, and N_B is the Bond number.</p> $u_{gu} = \frac{1.85(1 - \alpha C_0)K \left[\frac{g\sigma_{gl}(\rho_l - \rho_g)}{\rho_l^2}\right]^{1/4}}{\alpha C_0 \sqrt{\frac{\rho_g}{\rho_l}} + 1 - \alpha C_0} \quad \text{for a vertical wellbore}$ <p>K is a smooth transition function defined as:</p> $K = \begin{cases} 1.53 & \alpha \leq 0.06 \\ 1.53 + \frac{C_0 K_u - 1.53}{2} \left[1 - \cos\left(\pi \frac{\alpha - 0.06}{0.15}\right)\right] & 0.06 \leq \alpha \leq 0.21 \\ C_0 K_u & \alpha \geq 0.21 \end{cases}$	(A 1)	[11, 13]	
$C_0 = 1 + 0.2(1 - X) \left(\frac{gd_i \rho_l^2}{m^2}\right)^{0.25}$ <p>for $\alpha \geq 0.1$ m is the mass velocity.</p> $C_0 = 1 + 0.2(1 - X) \quad \text{for } \alpha < 0.1$	$u_{gu} = 1.18 (1 - X) \left[\frac{g\sigma_{gl}(\rho_l - \rho_g)}{\rho_l^2}\right]^{1/4}$	(A 2)	[19, 20]
$C_0 = 1.1 \quad \text{for } m \geq 200$ $C_0 = 1.54 \quad \text{for } m < 200$ <p>m is the mass velocity</p>	$u_{gu} = 1.18 \left[\frac{g\sigma_{gl}(\rho_l - \rho_g)}{\rho_l^2}\right]^{1/4}$	(A 3)	[19, 20]
$C_0 = 1.2$	$u_{gu} = 1.53 \left[\frac{g\sigma_{gl}(\rho_l - \rho_g)}{\rho_l^2}\right]^{1/4}$	(A 4)	[2]